TU Delft

Delft University of Technology

Underwater carbonation of alkali-activated slag pastes

Liu, Chen; Zhang, Yu; Liang, Minfei; Li, Zhenming; Ye, Guang

DOI
10.1016/j.conbuildmat.2024.137967

Publication date
2024

Document Version
Final published version

Published in
Construction and Building Materials

Citation (APA)
Liu, C., Zhang, Y., Liang, M., Li, Z., & Ye, G. (2024). Underwater carbonation of alkali-activated slag pastes. *Construction and Building Materials*, *445*, Article 137967. https://doi.org/10.1016/j.conbuildmat.2024.137967

Important note
To cite this publication, please use the final published version (if applicable).
Please check the document version above.

Copyright
Other than for strictly personal use, it is not permitted to download, forward or distribute the text or part of it, without the consent of the author(s) and/or copyright holder(s), unless the work is under an open content license such as Creative Commons.

Takedown policy
Please contact us and provide details if you believe this document breaches copyrights.
We will remove access to the work immediately and investigate your claim.

This work is downloaded from Delft University of Technology.
For technical reasons the number of authors shown on this cover page is limited to a maximum of 10.

Construction and Building Materials 445 (2024) 137967

Contents lists available at ScienceDirect

Construction and Building Materials

journal homepage: www.elsevier.com/locate/conbuildmat

Underwater carbonation of alkali-activated slag pastes

Chen Liu [a], Yu Zhang [a], Minfei Liang [a], Zhenming Li [b,c,*], Guang Ye [a,**]

[a] Department of Materials and Environment (Microlab), Faculty of Civil Engineering and Geoscience, Delft University of Technology, 2628 CN Delft, Netherlands
[b] School of Civil and Environmental Engineering, Harbin Institute of Technology, 518055 Shenzhen, China
[c] Guangdong Provincial Key Laboratory of Intelligent and Resilient Structures for Civil Engineering, Harbin Institute of Technology, 518055 Shenzhen, China

ARTICLE INFO

Keywords:
Carbonation
Alkali-activated slag
Water immersion
Leaching
Nanoindentation

ABSTRACT

Carbonation of alkali-activated slag (AAS) materials has been primarily concerned in atmospheres with gaseous CO_2. This study, by contrast, highlights that AAS pastes would also be carbonated under tap water immersion. Calcite is the main CO_2-bear phase in both sodium hydroxide- and sodium silicate-activated AAS pastes, and the paste pre-cured for a longer curing period shows more severe carbonation. Additionally, calcium carbonate can densify the deteriorated microstructure of sodium hydroxide-activated paste caused by long-term leaching. The indentation modulus of pastes subjected to tap water immersion is higher than those under deionized water immersion. The uptake of CO_3^{2-} by hydrotalcite (Ht) and gels is also detected, resulting in the formation of Ht-CO_3 and decalcification of gels. Due to the synergistic effect of leaching and carbonation, a characteristic layered distribution of pastes close to the exposure front is observed, comprising the carbonated layer, transitional (carbonated + leached) layer, and leached layer, progressing from the outermost to the inner regions. Eventually, the kinetics of underwater carbonation, as well as the discrepancy between dry and underwater carbonation, is revealed.

1. Introduction

The development of cement-free binders is a promising approach for manufacturing sustainable building materials, as they have the potential to substantially decrease CO_2 emissions from clinker production [1,2]. Granulated blast furnace slag, a prominent by-product of iron-making, has been widely utilized in the production of alkali-activated materials (AAMs) for several decades. These binders have been confirmed to exhibit outstanding mechanical properties, heat resistance, and chemical corrosion [3]. However, when it comes to carbonation, one of the most significant challenges in reinforced composites, AAS materials appear to be less robust than Portland cement materials, due to the unique reaction chemistry involved [4].

Fick's law is typically regarded as the fundamental governing equation for describing the diffusion of CO_2 in cementitious materials [5]. Due to the gradient of CO_2 concentrations, CO_2 molecules can migrate into the matrix of materials and then hydrolysis to HCO_3^- and CO_3^{2-} ions following the reactions of $CO_2 + OH^- \rightarrow HCO_3^- \rightarrow CO_3^{2-} + H^+$ [6]. In the Portland cement system, portlandite is one of the main reaction products during cement hydration, which can react with CO_3^{2-} ions to the formation of calcium carbonate [7,8]. This process can not only enhance the chemical binding of CO_2, but dense the microstructure of cement pastes, which can partly decelerate the diffusion of CO_2 [9,10]. In AAS systems, however, as the Ca content of slag is considerably lower than that of clinker, portlandite is scarcely formed in AAS materials [11]. As a result, a limited amount of calcium carbonate can be generated, which might be a weakness for CO_2 resistance compared to cementitious materials. Moreover, the main reaction product C-(N-)A-S-H gels in AAS systems is also different from C-(A-)S-H gels in cementitious systems in terms of elemental ratios. Normally, the Ca/Si ratio of C-(N-)A-S-H gels is lower than that of C-(A-)S-H gels. It was reported that the gel with a low Ca/Si ratio is more susceptible to decalcification [12,13]. An extensive decalcification of gels may result in deteriorated microstructure and cracking potential induced by carbonation shrinkage[14-16]. Fortunately, hydrotalcite, as the second major reaction product in AAS systems, can show CO_2 binding capacity and exceptional stability upon being carbonated. It was reported that a higher content of MgO in slag contributes to a lower carbonation penetration depth of AAS pastes [17].

Exposure condition is a critical factor governing the carbonation

* Corresponding author at: School of Civil and Environmental Engineering, Harbin Institute of Technology, Shenzhen, China.
** Corresponding author.
E-mail addresses: zhenmingli@hit.edu.cn (Z. Li), G.Ye@tudelft.nl (G. Ye).

https://doi.org/10.1016/j.conbuildmat.2024.137967
Received 27 March 2024; Received in revised form 13 May 2024; Accepted 16 August 2024
Available online 21 August 2024
0950-0618/© 2024 The Authors. Published by Elsevier Ltd. This is an open access article under the CC BY license (http://creativecommons.org/licenses/by/4.0/).

Table 1
Chemical composition of slag measured by XRF (wt%).

	CaO	Al_2O_3	SiO_2	MgO	Fe_2O_3	SO_3	K_2O	TiO_2	other	LOI
Slag	38.28	13.9	32.19	9.52	0.31	1.52	0.51	1.27	1.17	1.33

LOI: loss on ignition

resistance of materials. The natural atmosphere (0.04 vol%) is mostly utilized in some earlier publications [18,19], as it closely resembles real-life service conditions. However, the diffusion of CO_2 under such conditions is very low, posing challenges to predicting the penetration depth of CO_2 within the materials in the long term. To address this issue, accelerated carbonation regimes (normally 3 vol%) have been developed. In the case of cement binders, the phase assemblage of reaction products upon accelerated carbonation is comparable to that upon natural carbonation [20–22]. For AAS binders, however, 3 vol% is seemingly over-aggressive, as evidenced by the detection of sodium bicarbonate in the pore solution during accelerated carbonation. This is different from that in natural carbonation, where sodium carbonate is the main phase in the pore solution [23]. Therefore, a moderate CO_2 concentration of 1 vol% is recommended in accelerated carbonation tests for AAS materials [23]. Accordingly, researchers have applied this method to conduct intensive investigations at gel [24], paste [25,26], mortar [27] and concrete [27] scales.

Besides atmosphere carbonation, CO_2 can also dissolve in rivers, oceans, groundwater and moisture [28], where underwater carbonation can occur [29]. There are several literatures dealing with the durability of AAS under submerged or moist conditions, and most of them were concentrated on the impact of leaching [11,30,31]. Underwater carbonation of AAS materials has seldom been studied. The investigation of this phenomenon is crucial for gaining further insights into the impact of environmental water on the property of AAS materials and for evaluating their long-term durability when exposed to aqueous conditions.

In this study, AAS pastes activated by sodium hydroxide and sodium silicate solutions were initially sealed for 7 or 28 days and then exposed to tap water immersion for another 180 days. To begin with, the phase assemblage of AAS pastes with and without immersion was determined by X-ray diffraction (XRD) and thermogravimetric analysis (TGA), and the structural change of gels was identified by Fourier-transform infrared spectroscopy (FTIR). Then, the morphology and the chemical composition of pastes at different exposure depths were observed and determined using a scanning electron microscope (SEM) with energy-dispersive X-ray spectroscopy (EDX). Furthermore, nanoindentation tests were carried out to understand the change of micro-mechanical properties of water-immersed AAS pastes with and without carbonation. Thermodynamic modelling was performed to explain the above experimental results. Finally, based on the experimental and modelling results, a schematic representation was given to specify the kinetics of underwater carbonation of AAS pastes.

2. Materials and methods

2.1. Raw materials

The chemical composition of slag, as determined by a Panalytical Axios Max WD-XRF spectrometer, is presented in Table 1. The particle size distribution of slag was examined by a laser diffraction analyzer, covering a range from 0.1 to 50 μm with a d 50 of 17.9 μm.

NaOH solution (solid content: 50 wt%) and Na_2SiO_3 solution (100 g containing 8.25 g Na_2O, 27.5 g SiO_2, and 64.25 g water) were used for activator preparation. The NaOH (NH) activator was produced by combining NaOH solution with demineralized water, whereas the Na_2SiO_3 (NS) activator was prepared by mixing Na_2SiO_3 solution, NaOH solution, and demineralized water.

Table 2
Mixture proportions of AAS pastes.

	Slag (g)	SiO_2 (mol)	Na_2O (mol)	Water (g)
NH-activated (NH)	1000	0	0.8	430
NS-activated (NS)	1000	0.8	0.8	430

2.2. Sample preparation

Table 2 presents the mixture proportions of AAS pastes. Both NH and NS pastes were prepared using a constant Na_2O/slag weight ratio of 4.96 %. The fresh mixtures were initially blended for one minute at a low speed and then at a high speed mixing for one minute using a Hobart mixer. For XRD, TGA, FTIR, and EDX tests, the fresh AAS pastes were first sealed for 7 or 28 days (T = 20 °C) and then crushed into small pieces (2 mm - 4 mm). These crushed samples were exposed to weekly refreshed tap water (T = 20 °C, supplied by Oasen in the Netherlands, Ca: 44 mg/L) for another 7, 28, 90, and 180 days. The samples were named in the format of "As + Bw", which indicates that the sample was first sealed (s) for A days and then submerged in tap water (w) for B days. In terms of the nanoindentation test, the cylindrical sample (ϕ 20 mm × 20 mm) was prepared and sealed for 7 and 28 days. Subsequently, the cylinders were immersed in deionized and tap water for 90 days, with the side sealed by aluminium taps.

2.3. Methodology

2.3.1. Experimental characterizations

To analyze the change of phase assemblage and gel structure in AAS pastes with and without tap water immersion, XRD, TGA, and FTIR tests were employed. The piece samples were pulverized into fine powder in isopropanol solution, which aims to arrest the reaction of slag by the solvent exchange method [32]. This method allows for the extraction of free water from the sample while retaining the chemically bound water and physically absorbed water.

XRD was carried out using a Bruker D8 Advance diffractometer, with CuKα (1.54 Å) radiation. The scanning angles ranged from 5° to 70°, with a step size of 0.041°. To quantify the calcium carbonate content in water-immersed AAS pastes, Rietveld refinement [33] was carried out by a BMGN-based program called Profex. 10 wt% of silicon was introduced as the internal standard to hydration-arrested AAS paste powder.

TGA was conducted on a Netzch TG-449-F3-Jupiter, equipped with a mass spectrometer (MS), under an argon atmosphere. Approximately 32.5 mg of each sample was heated from 40 to 1000 °C at a heating rate of 10 °C/min in a crucible. The mass loss resulting from the emission of CO_2 and H_2O was monitored during the heating process. FTIR was performed employing a Spectrum TM 100 Optical ATR-FTIR spectrometer. The wavelength of the spectrum extended from 600 to 4000 cm^{-1} with a resolution of 4 cm^{-1}.

An FEI QUANTA FEG 650 ESEM equipped with an EDX detector was employed to characterize the morphology and elemental composition of AAS pastes. The reaction of 2–4 mm sealed and immersed piece samples at designated ages was arrested following the procedures mentioned above [32]. Then, the samples were dried and then impregnated using epoxy resin. The epoxy-embedded samples were polished with sandpapers and polishing clothes (down to 1 μm). Coating with carbon was necessary to improve the quality of images. The samples were observed under a working distance of 10 mm and an accelerating voltage of 10 kV

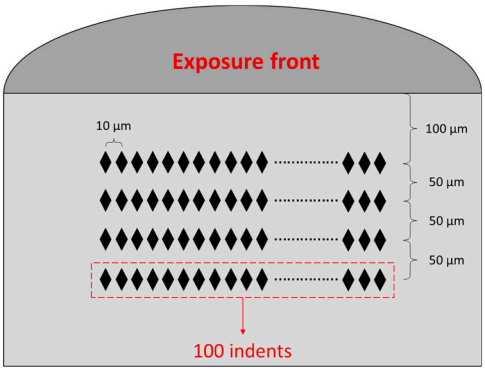

Fig. 1. Schematic illustration of the working area of nanoindentation tests.

at the BSE model.

To compare the effect of underwater carbonation on the micromechanical properties of AAS pastes, nanoindentation tests were performed using a G200 Nano-indenter with a continuous stiffness measurements (CSM) module near the exposure front of NH pastes. The NH cylinders were first sealed for 28 d, after which the sides were sealed by taps. Subsequently, the cylinders were immersed in deionized and tap water, respectively. After 90 d of immersion, the cylinders were vertically cut through the top and bottom surfaces. During the nanoindentation test, the working area was specifically chosen in the middle of the cross-section near the exposure front of cylinders, as presented in Fig. 1. An array of 4 × 100 indentations at a spacing of 50 μm was performed to cover an area of 150 μm × 1000 μm near the exposure front of samples. The distance between the first row of indentations and the exposure front of the samples was 100 μm. Each indent was made to a depth of 500 nm at a strain rate of 0.05 s^{-1}, with a harmonic frequency of 45 Hz and a CSM oscillation of 2 nm. An average depth from 100 to 500 nm was selected to probe the micromechanical properties of phases in AAS pastes [34].

2.3.2. Thermodynamic modelling

A Gibbs free energy minimization program, GEM-Selekor [35,36], was applied to simulate the change of phase assemblages of AAS pastes with the increase of additional water. The thermodynamic data from the PSI-GEMS database [37,38] was supplemented by the Cemdata18 database [39–41], including the solubility products of phases involved

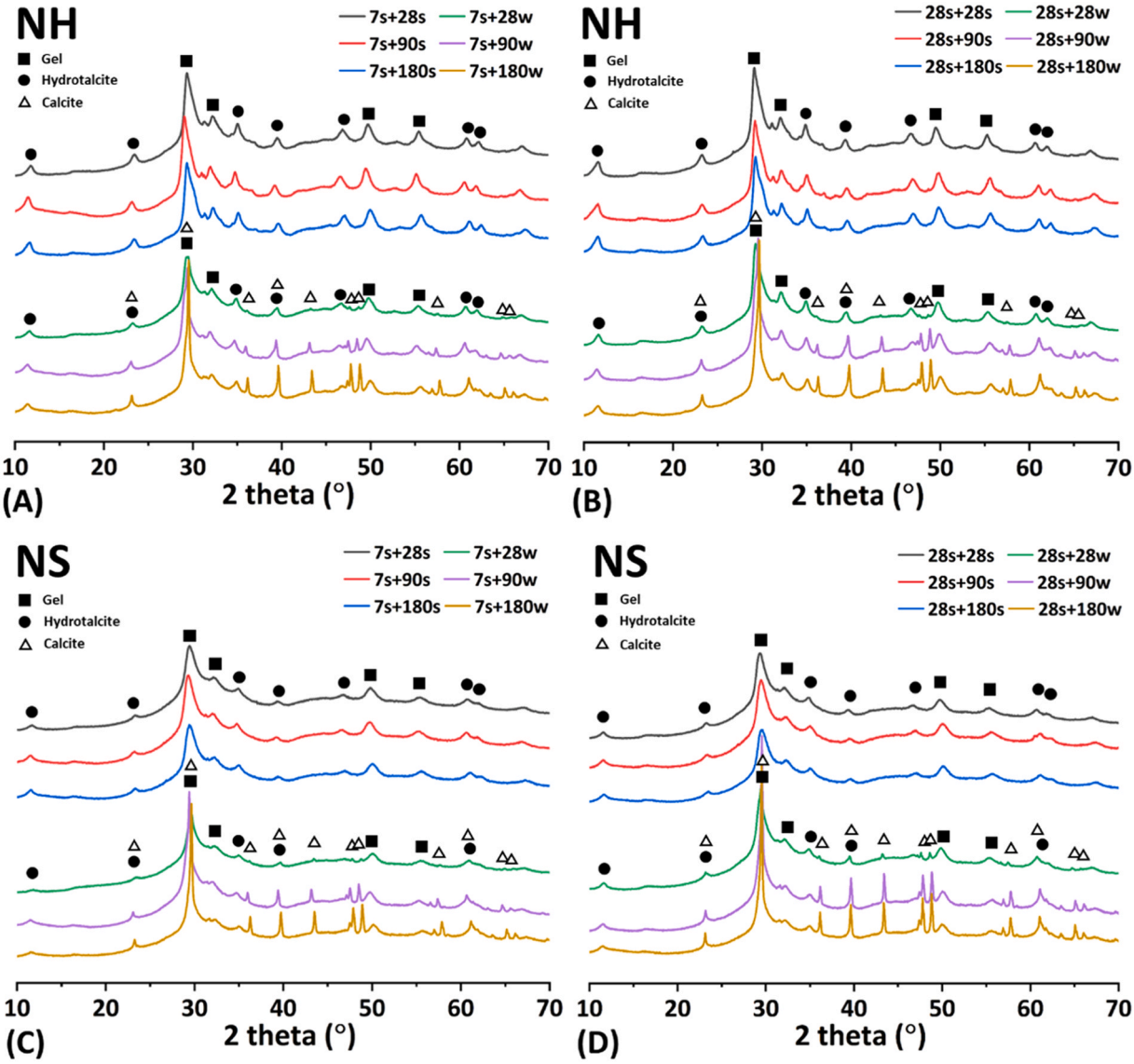

Fig. 2. XRD patterns of AAS pastes exposed to sealed and tap water-immersed conditions. Samples were first sealed (s) for 7 days and 28 days, and then half of the samples were transferred to tap water (w) immersion for another 28, 90, and 180 days.

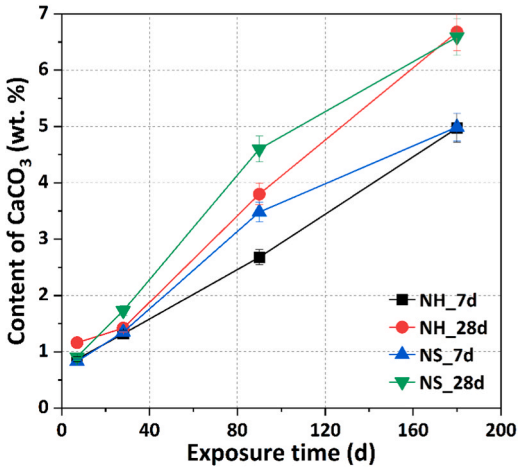

Fig. 3. Content of calcium carbonate in NH and NS pastes as a function of exposure time. "7 d" and "28 d" in the legend refer to the pastes pre-cured for 7 and 28 days under sealed conditions.

in this study. The thermodynamic model for calcium (sodium) aluminosilicate gels (CNASH_ss) proposed by Myers et al. [42] was used to mimic the gels formed in the AAS pastes. The hydrotalcite-like phase was described by the MgAl–OH–LDH_ss with three Mg/Al ratios (2, 3 and 4) [43]. The leaching process of AAS pastes was simulated at 20 °C.

3. Results

3.1. XRD

Fig. 2 shows the XRD pattern of 7 and 28 d AAS pastes exposed to sealed and tap water-immersed conditions for 28, 90 and 180 d. In general, two major reaction products i.e., C-(N-)A-S-H gels (14 Å tobermorite (PDF# 00–029–0331), 11 Å tobermorite (PDF# 04–017–1028) and 9 Å tobermorite (PDF# 04–012–1761)), and hydrotalcite (Ht) are identified in sealed AAS pastes. The intensity of the characteristic peak of gels is more pronounced in NH samples than in NS ones. This can be ascribed to the higher Ca/Si ratio in the gels formed in the NH system (Fig. 8), which contributes to forming more crystallized gels [44,45]. Besides, the signal of the Ht in NS pastes is also weaker than in NH pastes. On one hand, the pH of the pore solution in the NS system might be lower than that in the NH system at the same alkali dosage, which hinders the reaction of slag and the formation of Ht [45]. On the other hand, the presence of silicate in NS activator can promote the formation of gels, which relatively lowers the content of Ht in NS pastes.

Moreover, calcite is identified as a major phase of $CaCO_3$ polymorphs in the samples exposed to tap water, and the intensity of which increases over time, as shown in Fig. 2. Similar findings were also reported in [11]. They attributed this to the reaction between dissolved CO_2 and Ca ions in the alkali leachate. Due to the poor crystallization of C-(N-)A-S-H gels and unreacted slag, it is challenging to precisely determine their content by the XRD Rietveld method. Therefore, we quantify the content of calcium carbonate in immersed pastes, as shown in Fig. 3. It is observed that the content of calcium carbonate in both NH and NS pastes increases with time. Interestingly, the amount of $CaCO_3$ in both pastes pre-sealed for 28 days is constantly higher than those pre-sealed for 7 days. The Ca in calcium carbonate is derived from both tap water and AAS pastes. Due to the same tap water used in all samples, the distinction primarily arises from the AAS paste. It is predictable that the reaction degree of slag at 28 d is higher than that at 7 d under sealed conditions, which indicates a higher abundance of Ca in 28 d AAS samples. In spite of a denser microstructure of 28 d pastes, the availability of Ca plays a more decisive role.

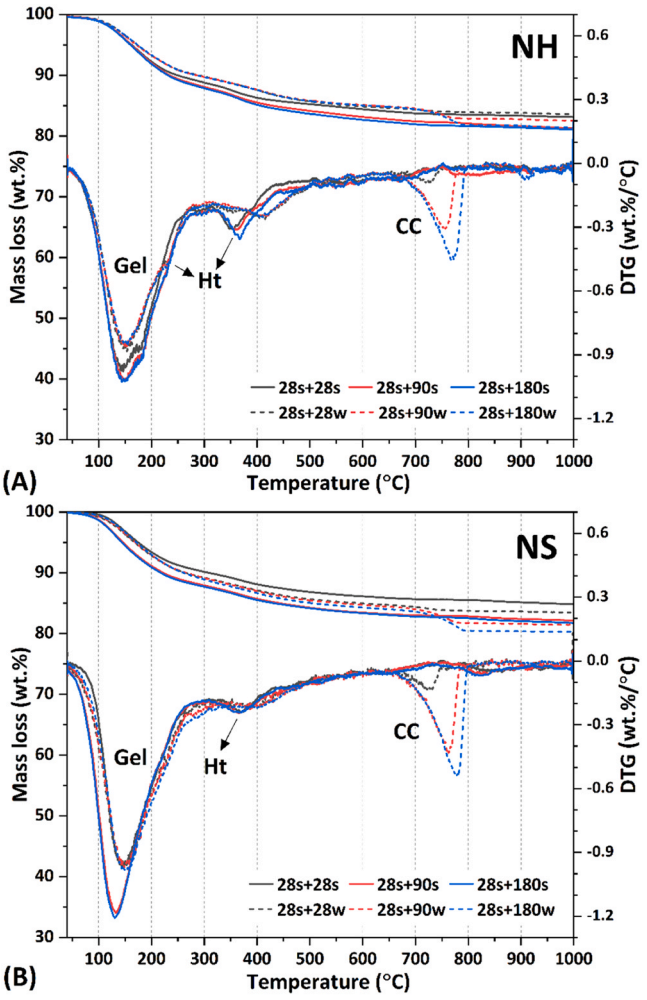

Fig. 4. TG and DTG curves of 28 d AAS pastes exposed to sealed and tap water conditions for 28, 90 and 180 days. Ht: hydrotalcite; CC: calcium carbonate.

3.2. TGA

Given that the typical divergence between the samples with different pre-curing ages has been reflected by XRD tests, the subsequent measurements only focus on the sample pre-sealed for 28 d. Fig. 4 shows the TG and DTG results of 28 d AAS pastes after 28, 90 and 180 days of exposure. Three distinctive peaks are observed within the temperature ranges of 40–300 °C, 300–500 °C and 650–800 °C, corresponding to the weight loss of C-(N-)A-S-H gels, Ht, and calcium carbonate (CC), respectively. Under sealed conditions, the weight loss peak of gels in NS pastes is more pronounced than that in NH pastes, implying a higher gel content in the NS system. Besides, the presence of a hump around 400 °C, coupled with a small shoulder located at 250°C, indicates a higher content of hydrotalcite in NH paste. This is in agreement with XRD results (Fig. 2), attributed to the higher alkalinity of the pore solution in the NH system, which facilitates the dissolution of Mg and Al from slag and the formation of Ht.

In accordance with the XRD data, decomposition peaks of calcium carbonate are detected in immersed samples. The intensity increases with the extension of immersion time, indicating an increasing amount of calcium carbonate in AAS pastes. Besides, the average decomposition peak of calcium carbonate also increases with exposure time, which suggests an increasing stability and crystallinity of calcium carbonate [46]. As reported in [24,47], ACC (amorphous calcium carbonate) emerges as a critical CO_2-bearing phase in AAS pastes upon dry carbonation (natural or accelerated carbonation), which is decomposed

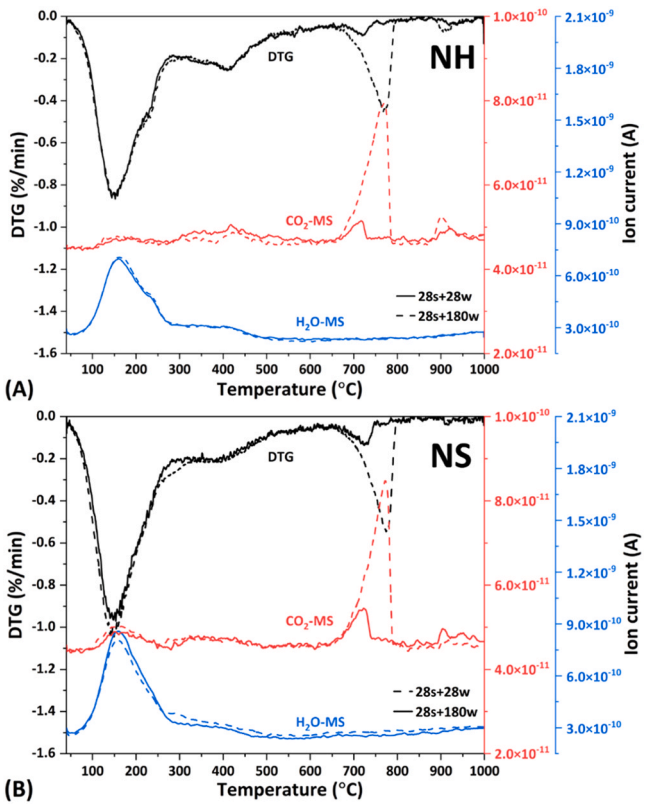

Fig. 5. DTG, H_2O- and CO_2- MS curves of 28 d AAS pastes after 28 and 180 days of tap water immersion. The solid lines and dash lines refer to the samples exposed for 28 and 180 days, respectively.

at a relatively low-temperature range of 400–600°C. However, ACC is rarely detected in underwater carbonated pastes. This indicates that the underlying mechanism behind underwater carbonation is different from that of dry carbonation.

Furthermore, there also exists some changes regarding gels and hydrotalcite after exposure. As for gels, the content in paste after water immersion is much lower than that under sealed conditions. This is correlated to gel decomposition [11] and the increased content of calcium carbonate to some extent. In the case of Ht-like phases, although the content seems to show no obvious change, an elevated decomposition temperature is identified in exposed samples. Bernard et al. [48] investigated the chemical stability of hydrotalcite with different interlayered anions. Ht-CO_3 shows the highest disintegration temperature and the most intensive XRD reflection among Ht-like phases modified by OH^-, Cl^-, NO_3^-, CO_3^{2-} and SO_4^{2-} anions. Thus, the elevated decomposition temperature of Ht is related to the substitution of OH^- by CO_3^{2-} in the interlayer. To verify this hypothesis, TG-DTG-MS analysis was conducted.

The DTG, H_2O and CO_2 MS curves of AAS pastes exposed to tap water for 28 and 180 days are demonstrated in Fig. 5. As stated in Section 2.3.1, TGA-MS measurements were performed on samples with equal weight, ensuring that the ion current in is dependent on the content of OH^- or CO_3^{2-} in the samples. The H_2O-MS curves are dominated by the hump at ~ 150 °C, representing the presence of chemical-bound water in gels. The hump in the range of 300–400 °C, along with a slight shoulder on the high-temperature side of the gel peak is also observed, which can be assigned to the weight loss of OH^- in the interlayer of hydrotalcite. In terms of CO_2-MS curves, in addition to the notable peak associated with the decomposition of calcium carbonate at 700–800 °C, the release of CO_2 also occurs from the gel and Ht-like phases at temperatures of 100–200 °C and 300–400 °C, respectively.

Typically, calcium carbonate is the primary CO_2-bearing phase in a

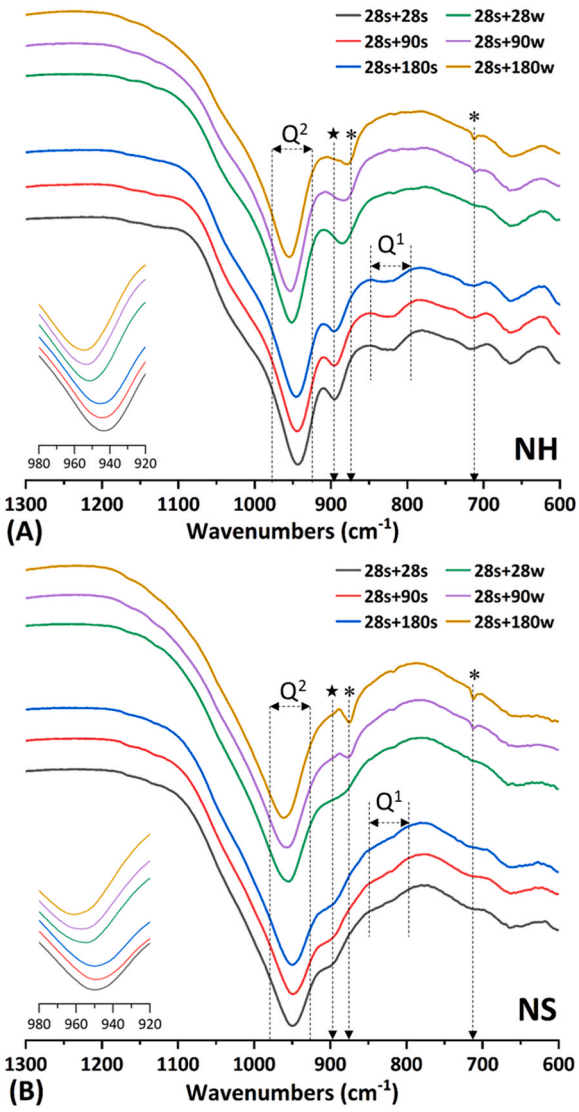

Fig. 6. FTIR spectra of 28 d NH and NS pastes exposed to sealed and tap water conditions with time. ★refers to the stretching of Si-O (OH-Si near Ca in bridging tetrahedra) [53]; * refers to the bending of CO_3^{2-} in carbonates [51]. The inset figure is an enlarged view at the region of 920–980 cm^{-1}.

Portland cement system upon carbonation [46,49], with a disintegration temperature starting from 500 °C. Additionally, two secondary phases are formed as well: Ht-CO_3 decomposing at 350–450 °C and carbonated AFm-like (monosulfate) phases decomposing at ~150°C. The layered structure of these two phases allows for the substitution of OH^- or SO_4^{2-} by CO_3^{2-} when they are exposed to a CO_2 atmosphere. In this study, the hump observed at 350–450 °C in Fig. 5 can be assigned to the formation of Ht-CO_3. The hump at 100–250 °C cannot be attributed to AFm-like phases due to the absence of characteristic peaks in the XRD results (Fig. 2). It is speculated that the release of CO_2 in this temperature range is likely due to the carbonates trapped by gels, as gels have a high specific area, contributing to physically absorb carbonate ions [50]. It is worth noting that the gel-related CO_2-MS peaks in NS samples are more evident than those in NH samples. This is mainly due to the higher content and more compact packing of gels in NS paste, allowing for greater capture of carbonate ions.

3.3. FTIR

Fig. 6 shows the FTIR results of AAS pastes with the exposure time.

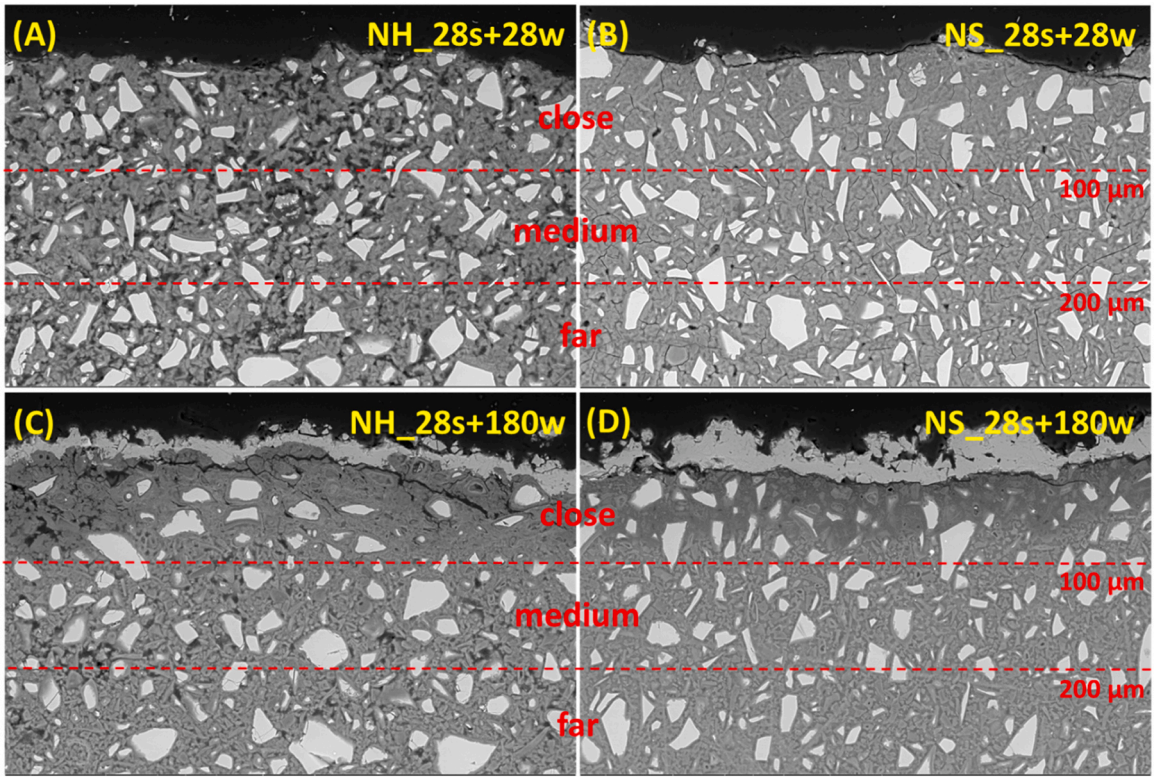

Fig. 7. Cross-section of the exposure front of 28 d AAS samples exposed to tap water for 28 and 180 days. The paste is divided into three zones in terms of the distances (0–100 μm, 100–200 μm and 200–300 μm) from the edge, namely "close", "medium" and "far".

According to [51], the sharp band at ~950 cm^{-1} corresponds to the stretching vibration of Si-O bonds, representing the Q^2 site in the gel structure. The wavenumber associated with Q^2 is indicative of the degree of polymerization of the gels, with a higher wavenumber suggesting a higher polymerization degree of gels. In the case of the sealed AAS pastes, the NS paste shows a higher wavenumber in the Q^2 unit than the NH one. This is because a lower Ca/Si ratio (Fig. 9) is advantageous for improving the polymerization degree of gels [52]. As shown in the inset figure of Fig. 6, both NH and NS pastes show comparable wavenumbers of Q^2 under sealed conditions with time, respectively. However, the paste immersed in tap water shows a higher wavenumber of Q^2 than the sealed paste, and the wavenumber of Q^2 increases with immersion time. This means that the gel after immersion obtains a higher polymerization degree.

This increased polymerization degree of gels can be ascribed to gel decalcification induced by both leaching and carbonation. As found in our previous work [30], Na shows high mobility in C-(N-)A-S-H gels subjected to water immersion, and the leaching of Na can trigger the movement of intralayer Ca to the interlayer. This will lead to the decalcification in the intralayer and increased polymerization degree of gels. On the other hand, the interlayer Ca can also leach away from gels or react with carbonate ions to the formation of calcium carbonate [12]. With the decrease of Ca content in the interlayer, the structure of gels will change gradually to rebalance the change in basal spacing, which results in a more cross-linked structure as well.

Moreover, the band near 900 cm^{-1} is assigned to the stretching vibration of Si-O bonds near Ca in bridging tetrahedra [53]. Due to the lower content of Ca in the gel of the NS system, the signal of this band in sealed NS samples is much weaker than in sealed NH ones. Additionally, this peak appears to be less evident in the paste after tap water exposure, as an indicator of gel decalcification. The bending of CO_3^{2-} in carbonates is detected at ~875 cm^{-1} [51] and ~710 cm^{-1} [54] in the exposed pastes. A hump concerning Q^1 sites in gels from 800 to 850 cm^{-1} is identified apparently in sealed NH pastes [51], which implies a more significant content of Q^1 and a lower polymerization degree of gels than NS pastes. It should be noted that this hump seems to be flat upon tap water exposure in NH samples, indicating a more cross-linked gel structure.

3.4. SEM and EDX

Fig. 7 shows the cross-section of exposure front of AAS pastes subjected to tap water immersion. To facilitate analysis and description, the pastes near the edge were divided into three sections, namely "close", "medium" and "far", representing different distances (0–100 μm, 100–200 μm and 200–300 μm) from the exposure front. Comparing Fig. 7A and B, it is evident that the NS paste shows a denser microstructure than the NH one. This is mainly due to the presence of soluble Si in the NS activator, which facilitates the formation of gels and the densification of microstructure [11,55]. The NH paste is more permeable and vulnerable to water intrusion. Firstly, the pH of the pore solution decreases as external water infiltrates the paste, which impedes the reaction of slag and the formation of reaction products [11]. Secondly, long-term water immersion leads to gel decomposition, further deteriorating the pore structure [11]. In contrast, the NS paste is relatively dense, and there is little distinction among the three regions after 28 d of immersion (Fig. 7B).

After being submerged for 180 days, notable differences are observed in both samples compared to those exposed for 28 days. The most evident change is the formation of a calcium carbonate layer surrounding the samples, as observed in Fig. 7C and D. Besides, it is interesting to note that the NH paste after 180 days of water immersion is denser than that after 28 d. On one hand, a prolonged hydration time promotes the formation of reaction products and the refinement of microstructure. On the other hand, the porous microstructure appears to be densified by calcium carbonate, particularly near the edge of pastes. This hypothesis will be further verified by EDX results.

Furthermore, several visible cracks are identified in the "close"

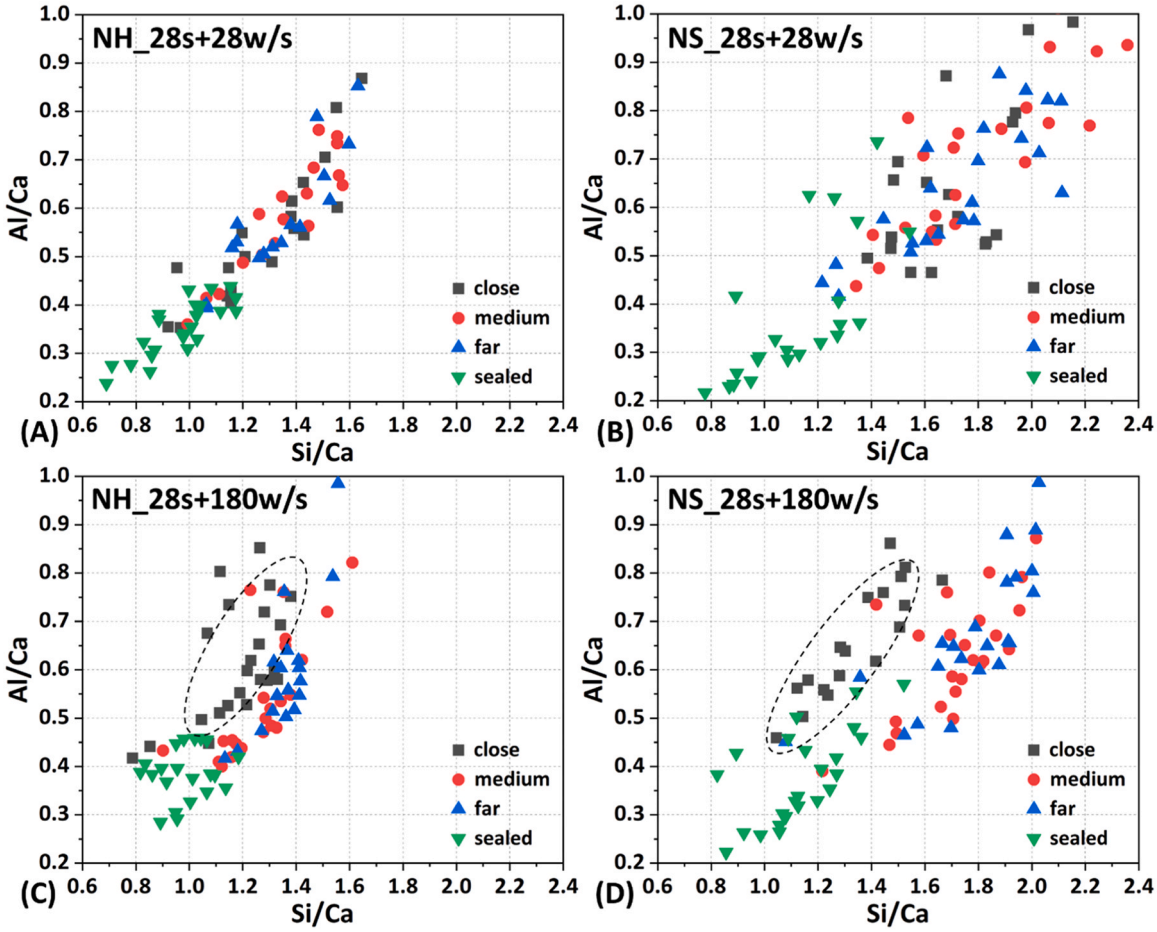

Fig. 8. Atomic ratios of Si/Ca against Al/Ca of 28 d AAS pastes subjected to tap water immersion and sealed curing for 28 and 180 days. The labels "close", "medium" and "far" represent the point analysis zones presented in Fig. 7, which are in the same water-immersed sample (w). "s" refers to the samples constantly exposed to sealed conditions.

region (Fig. 7C). Since the samples are constantly stored in water, the cracks identified near the exposure front are seemingly attributed to carbonation shrinkage instead of dry shrinkage [22]. Due to the dense matrix of the NS paste, even after 180 days of exposure, it remains hard to discern three regions in appearance, in addition to a darker "close" region than "medium" and "far" (Fig. 7D). This suggests that the average relative atomic mass of the pastes close to the surface is lower than the inner part, which is likely due to the leaching of ions and the carbonation of gels.

The atomic ratios of Si/Ca and Al/Ca in NH and NS pastes subjected to 28 and 180 days of tap water immersion and sealed curing are shown in Fig. 8. In general, the Si/Ca ratio of NH pastes is lower than NS pastes in sealed condition at the same age, due to the presence of soluble Si in NS alkali activator. Besides, the Si/Ca and Al/Ca ratios in both sealed pastes are lower than those in the paste exposed to water, regardless of exposure age, as an indicator of gel decalcification.

Moreover, as demonstrated in Fig. 8A and B, the atomic ratios of Si/Ca and Al/Ca in both pastes at "close", "medium" and "far" zones are intermixed and display minimal variation. Although the paste near the exposure front is subjected to gel decalcification, there remains limited change in the chemical composition at 28 d. This is coherent with the image in Fig. 7A and B, in which the morphology of the three sections exhibits invisible change. However, upon 180 d of exposure, the Si/Ca ratio of pastes at the "close" region (refer to the points in black dashed circles in Fig. 8C and D) presents a lower value than the "medium" and "far" regions, whereas the data points at "medium" and "far" zones still overlap. This suggests that the paste close to the exposure front contains a higher concentration of calcium. Due to the lower relative atomic mass of C than Si and Al, the carbonated gel typically shows a lower atomic mass and a higher greyscale than the uncarbonated gel. Therefore, the darker colour observed at the "close" zone in both NH and NS pastes (Fig. 7C and D), the elevated Ca/Si ratio can be attributed to a combination of gel and calcium carbonate.

Fig. 9 illustrates the atomic ratio of Al/Si with the variation of Mg/Si in AAS pastes exposed to immersion and sealed conditions. As reported in [56], a linear correlation between the Mg/Si and Al/Si ratios indicates the existence of ht-like phases while the intercept of the X-axis refers to the Al/Si ratio of inner gels in the rim of slag. It is demonstrated that the Al/Si ratio of gels is between 0.2 and 0.3 in both NH and NS systems and the slope representing the Mg/Al ratio in Ht-like phases remains unchanged after 180 days of exposure. This confirms that long-term tap water immersion cannot appreciably affect the chemical composition of Ht [48].

3.5. *Nanoindentation test*

As shown in Fig. 7**C** and **D**, it is evident that tap water has a more pronounced effect on the NH paste with a coarser microstructure than the NS paste. To better understand the impact of underwater carbonation on the micro-mechanical properties of AAS materials, nanoindentation tests were performed on tap water-immersed and deionized water-immersed NH pastes. Fig. 10A and B show the indentation modulus of NH pastes sealed for 28 days, followed by 90 days of deionized and tap water immersion, respectively, as a function of

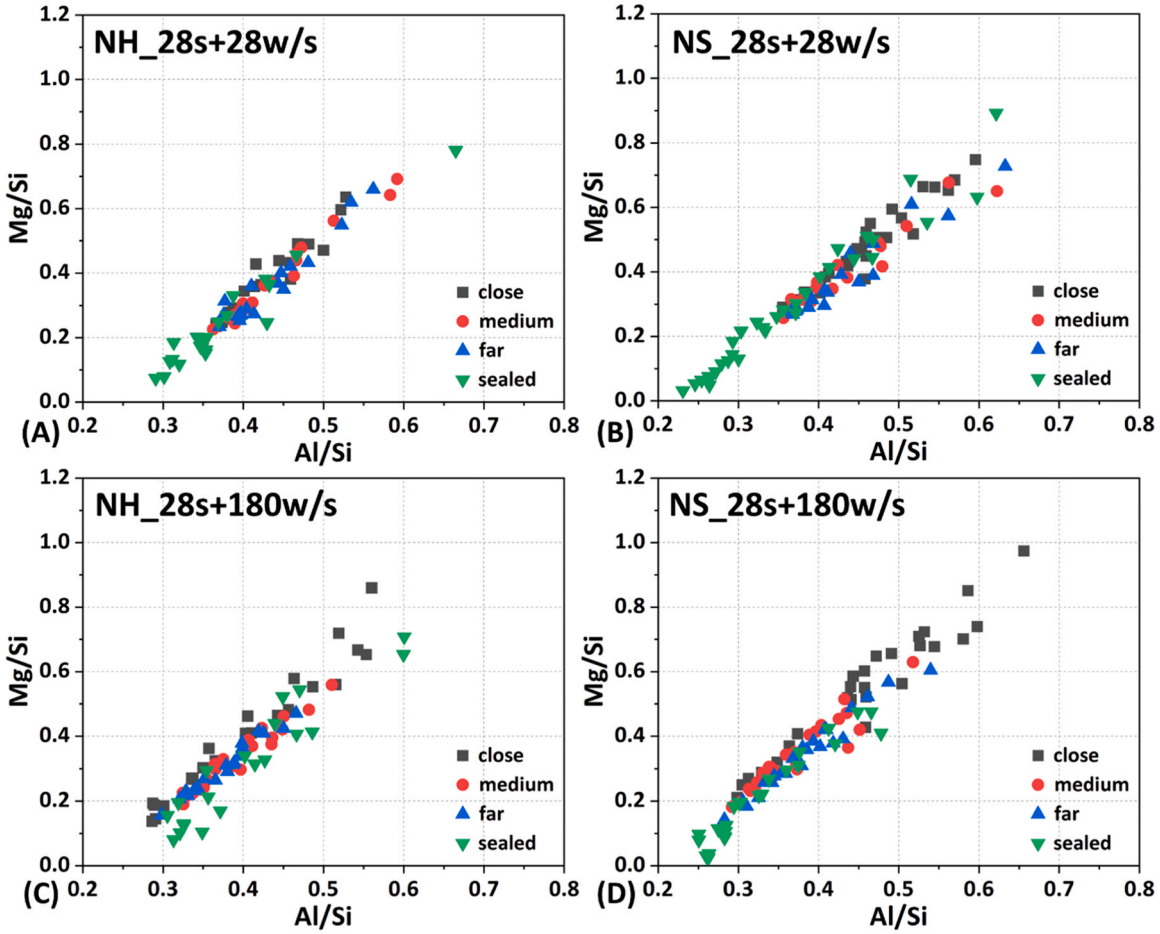

Fig. 9. Atomic ratios of Al/Si against Mg/Si of 28 d AAS pastes exposed to tap water and sealed conditions for 28 and 180 days. The labels "close", "medium" and "far" represent the point analysis zones presented in Fig. 7, which are in the same water-immersed sample (w). "s" refers to the samples constantly exposed to sealed conditions.

distances away from the edge. The samples undergoing deionized water immersion are prone to leaching problems. With the leaching of ions, the chemical environment surrounding gels has been changed, resulting in the gradual dissolution of the gels. This, in turn, leads to the development of a porous microstructure [11]. As shown in Fig. 10A, the indentation modulus of the paste at the "close" (100 μm) and "medium" areas (150 and 200 μm) is lower than that at the "far" region (250 μm). This is supported by the observation in Fig. A1A, in which the paste at the "close" and "medium" regions shows a more porous structure than that at the "far" region.

However, the samples exposed to tap water immersion not only suffer from leaching but also experience carbonation. As shown in Fig. A1B, the paste upon 90 days of tap water immersion shows a denser microstructure than that upon 90 days of deionized water immersion at the "close" and "medium" regions. This probably indicates that the leaching of Ca^{2+} ions promotes the formation of calcium carbonate, which can dense the porous microstructure caused by leaching. Correspondingly, the indentation modulus of the paste exposed to tap water in the "close" and "medium" regions is generally higher than that under deionized water immersion (Fig. 10B). Besides, the values for both NH and NS pastes at a distance of 250 μm are comparable, indicating a limited region affected by underwater carbonation. Interestingly, it is also observed in Fig. 10B that the indentation modulus of the "close" paste is lower than the pastes in the "medium" region. This disparity may be attributed to the fact that the paste closer to the exposure front experiences more significant carbonation, which results in lower mechanical properties than the relatively farther region to the exposure front. Despite this, the indentation modulus of tap water-immersed pastes is higher than that of deionized water-immersed pastes at 100 μm. This suggests that underwater carbonation can compensate for the adverse effect induced by gel carbonation, which is beneficial for higher micro-mechanical properties.

3.6. Thermodynamic modelling

For a further understanding of the leaching of AAS pastes subjected to water immersion, thermodynamic modelling was performed focusing on the NH paste as a representative case. Fig. 11 illustrates the phase assemblage and ion concentration of Ca^{2+} and $CaOH^{+}$ in the pore solution of NH paste with the reaction of slag. The content of C-(N-)A-S-H gels (CNASH_ss) and hydrotalcite-like phases (MgAl-OH-LDH_ss) increases as the increasing reaction degree of slag. Additionally, both the concentrations of Ca^{2+} and $CaOH^{+}$ in the pore solution, along with their increased rates, rise with the reaction of slag. This indicates that a higher reaction degree of slag contributes to an increased content of Ca in the pore solution. A higher concentration of Ca in 28 d samples contributes to a higher formation of calcium carbonate (Fig. 3).

Alisa et al. [57] investigated the effect of leaching on the phase assemblage of cement pastes blended with dolomite by thermodynamic modelling, using a cement-specific database (Cemdata14). Their findings revealed the decomposition of gels, portlandite, and ettringite in the presence of water. Herein, we studied the leaching in an AAS system using an extended database (Cemdata18). Fig. 12A shows the mass loss of the main reaction products (C-(N-)A-S-H gels and Ht-like phases) in

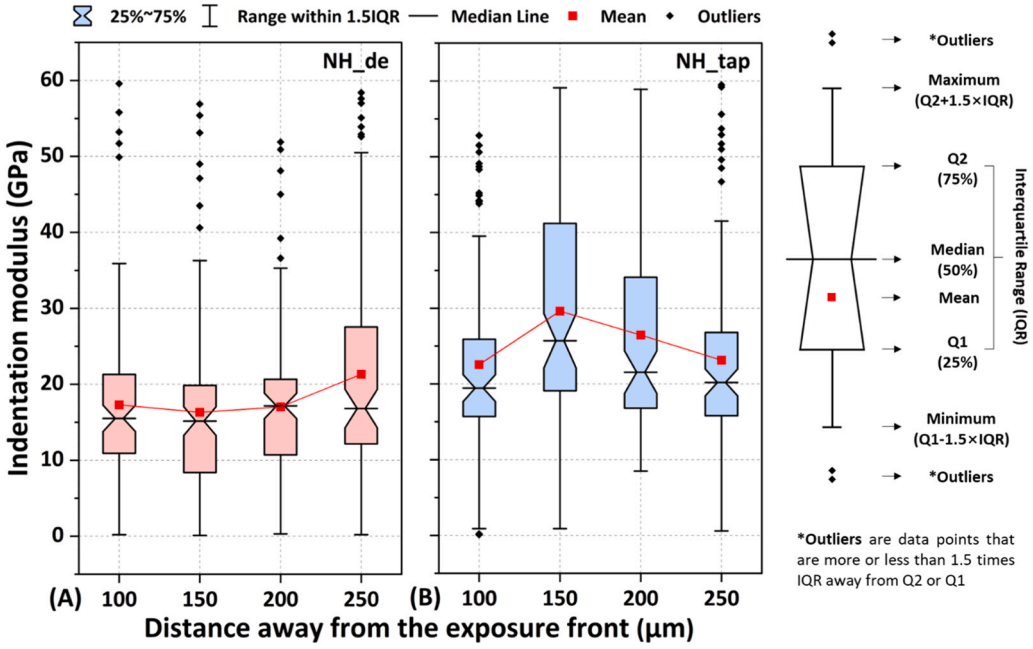

Fig. 10. Box plots of indentation modulus for the NH paste at different distances away from the edge of samples. (A) 28 d sealed NH pastes after 90 days of deionized water immersion ("de"); (B) 28 d sealed NH pastes after 90 days of tap water immersion ("tap"). In each box, the notch located at the median indicates the 50th percentile, while Q1 and Q2 denote the 25th and 75th percentiles, respectively. The whiskers extend to the maximum and minimum data points, which are within the 1.5 times interquartile range (IQR). The outliers are the data points that are more or less than 1.5 times IQR away from Q2 and Q1, which probably indicate the presence of slag or calcium carbonation and the region near pores.

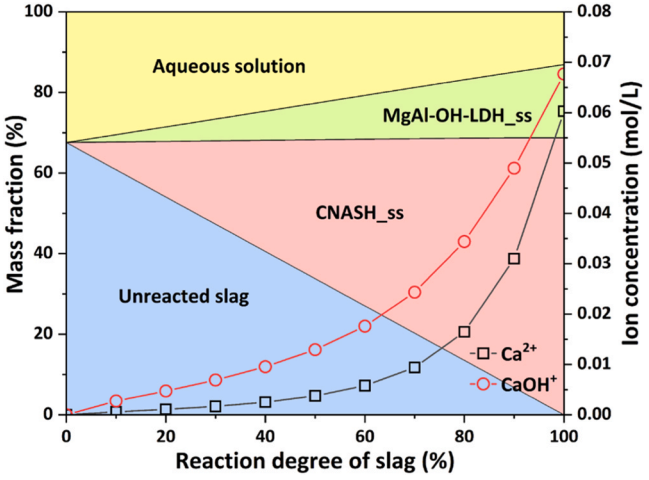

Fig. 11. Phase assemblage and concentrations of Ca^{2+} and $CaOH^{+}$ in the pore solution of NH paste with the reaction of slag.

the paste with the addition of water. The phase assemblage of the paste before water addition is determined based on the mixture design of the NH paste (Table 2) with a 50 % reaction degree of slag, representing a 28 d sealed NH paste [11]. In agreement with [30], the total mass of gels decreases with the increase of water addition, due to the continuous leaching of ions. The average Ca/Si ratio of C-(N-)A-S-H gels with the addition of water is plotted in Fig. 12B in red. The Ca/Si ratio decreases with the increase of additional water, which indicates that Ca is more mobile than Si in the gel of NH systems under leaching conditions. This result is consistent with the result in Fig. 8, in which the Ca/Si ratios of exposed pastes are lower than those of sealed ones. As for Ht, the total mass of the three types of phases remains relatively stable. The blue curve in Fig. 12B indicates a gentle increase in the Mg/Al ratio in the hydrotalcite-like phases gently increases from 2 to 2.14 as the dosage of water ranges from zero to ten thousand molars. This observation aligns well with the experimental results in Fig. 9, where the Mg/Al ratio of hydrotalcite remains unchanged after long-term immersion. By employing thermodynamic modelling, we can qualitatively study the leaching of AAS pastes in deionized water, however, there remain some limitations. On one hand, it fails to simultaneously consider both leaching and carbonation. On the other hand, this approach can only simulate the leaching of a system without the continuous reaction of slag.

4. Discussion

4.1. Characteristic layered distribution of pastes upon underwater carbonation

Fig. 13 presents the 28 d sealed NH paste upon 180 days of tap water immersion at a low magnitude. Combined with the EDX results (Fig. 8), the paste can be roughly divided into three parts: "carbonated zone", "carbonated + leached zone" and "leached zone" from the outmost to the inside. In the "carbonated zone", calcium carbonate is the main CO_2-bearing phase, recognized by its relatively bright greyscale. In the "carbonated + leached zone" (refer to the "close" region in Fig. 7), the voids (indicated by the red dashed circles in Fig. 13) caused by the spalling of slag during sample polishing are the most notable features distinguished from the other parts. The higher Ca/Si ratio of pastes in this region than the leached part suggests the presence of an intermixed phase consisting of calcium carbonate and gels (Fig. 8). The newly formed calcium carbonate can dense the porous microstructure induced by leaching, resulting in a higher indentation modulus (Fig. 10). The spalling of slag can be attributed to a reduced adhesive strength between the pastes and unreacted slag particles. Additionally, cracks are also observed in this zone, potentially due to carbonation shrinkage. In the "leaching zone" (refer to the "medium" and "far" regions in Fig. 7), the paste seems to be primarily influenced by leaching instead of carbonation, as the Ca/Si ratio of pastes is lower than that in both the "close" and "sealed" pastes (Fig. 8). The dominated influence of leaching at this

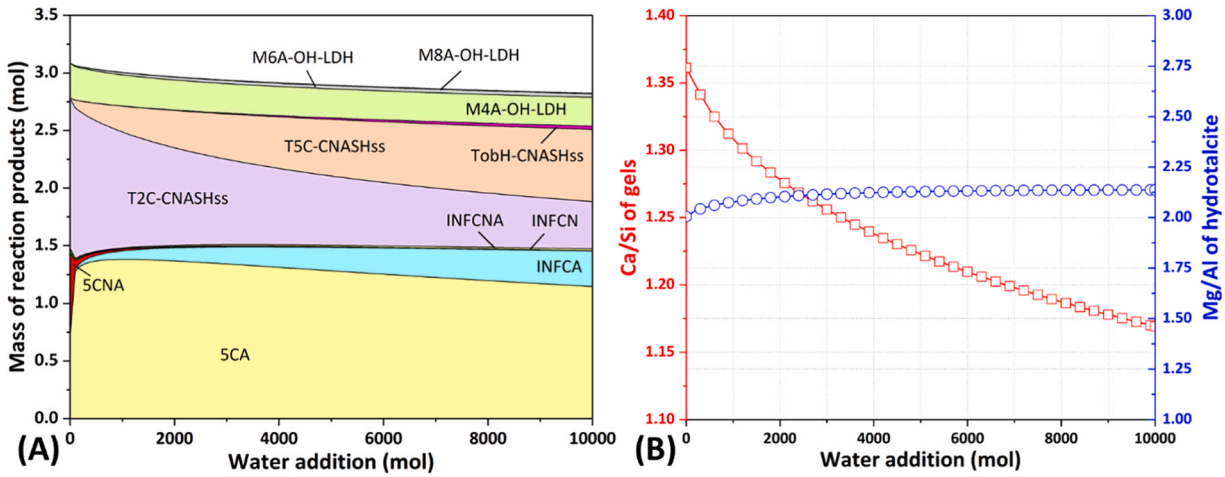

Fig. 12. (A) Mass change of C-(N-)A-S-H gels (5CA, 5CNA, INFCA, INFCN, INFCNA, T2C-CNASHss, T5C-CNASHss and TobH-CNASHss) [42] and hydrotalcite-like phases (M4A-OH-LDH, M6A-OH-LDH and M8A-OH-LDH) [39] in NH-activated pastes (1000 g slag, 0.8 M Na_2O and 430 g H_2O) with 50 % reaction degree of slag as a function of water addition. (B) Change of the Ca/Si ratio of C-(N-)A-S-H gels and the Mg/Al ratio of hydrotalcite-like phases with the addition of water.

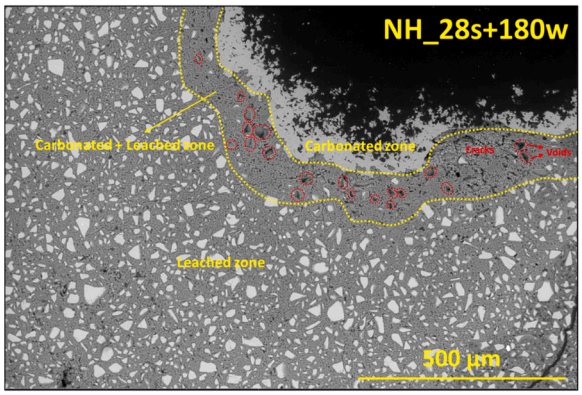

Fig. 13. A typical morphology of 28 d NH pastes exposed to tap water immersion for 180 days. The black part in the top right corner is the epoxy outside of the sample.

zone is further supported by the comparable nanoindentation modulus of pastes subjected to tap and deionized water in the "far" regions (Fig. 10). It should be noted that the thickness of each layer in Fig. 13 appears different from that shown in Fig. 7. On one hand, this is due to the variations in the severity of carbonation at different locations within the samples. On the other hand, the observed carbonation depth may not reflect the real thickness of the 3D shell structure due to different cutting angles. Notably, the characteristic layered distribution at the exposure front of NS pastes is not that evident compared to NH pastes (Fig. 7D). This is due to a much denser microstructure of the NS paste than the NH paste, resulting in a thinner affected region induced by leaching and carbonation.

4.2. *Kinetics of underwater carbonation*

To interpret the kinetics of underwater carbonation of AAS pastes, a schematic diagram is presented in Fig. 14. As shown in Fig. 14A, the leaching of alkali (earth) metal cations and OH^- ions from the pore solution is predominant at the early stages [11]. This is ascribed to the gradient of ion concentration between the pore solution and tap water. Then, the pH of the pore solution decreases while that of the external host solution increases [11]. An alkali condition promotes the hydrolysis reaction from H_2CO_3 to CO_3^{2-} ions in tap water and the absorption of gaseous CO_2 from the environment. These carbonate ions can then interact with Ca^{2+} to the precipitation of calcium carbonate in the tap

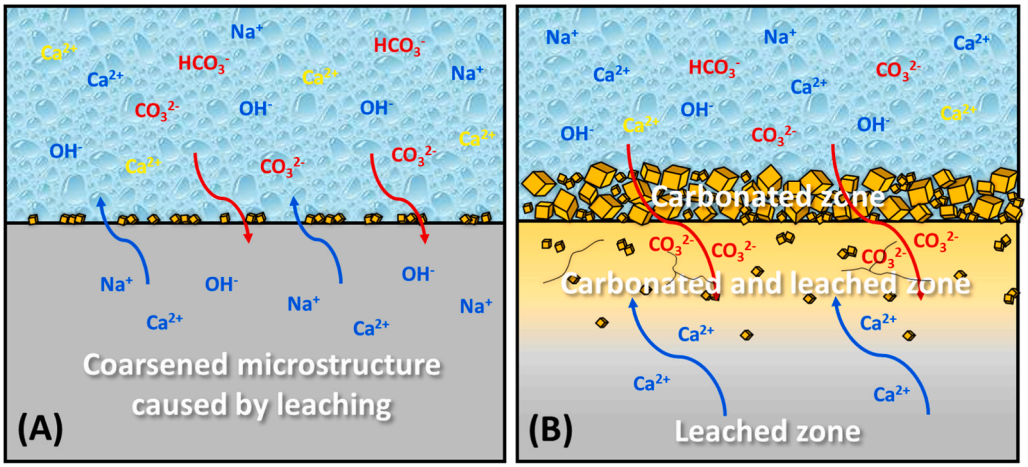

Fig. 14. A schematic diagram of the kinetics of underwater carbonation of AAS pastes subjected to tap water immersion. (A) and (B) refer to short-term and long-term exposure, respectively. The ions in blue derive from pastes. The Ca^{2+} ion in yellow represents the one in tap water. The CO_3^{2-} and HCO_3 ions in red refer to the hydrolytic CO_2 originating in the tap water or captured from the environment. The orange cube represents calcium carbonate.

water or on the surface of the samples. At this stage, the main source of Ca^{2+} for calcium carbonate formation is tap water, considering that the concentration of Ca in tap water (44 mg/L) is higher than that in the pore solution (approximately 20 mg/L in 28 d sealed NH/NS pastes [11]). As reported in [11], amounts of calcium carbonate are observed in the leachate. The presence of calcite is also detected after 7 and 28 days of immersion (Fig. 2), whereas they are insufficient to form a detectable calcium carbonate layer around the paste upon 28 days of exposure (Fig. 7A and B). Besides, with the progressive leaching of ions, the initial equilibrium between solid and liquid phases is disrupted, resulting in the decomposition of gels and the coarsening of the microstructure near the exposure front (Fig. 7A).

Fig. 14B shows the layered distribution of AAS pastes after long-term tap water immersion. More and more free Ca^{2+} ions migrate toward the exposure front over time. On one hand, leaching can lead to the decalcification of gels in the inner matrix, elevating the polymerization of the gel structure. On the other hand, the leached Ca^{2+} ions accumulate near the exposure front, reacting with CO_3^{2-} ions to the formation of calcium carbonate. This results in an increased Ca/Si ratio of pastes in the "carbonated + leached zone" than the "leached zone" (Fig. 8C and D) and the thickening of a calcium carbonate layer ("carbonated zone"). The newly formed calcium carbonate plays a role in densifying the coarsened microstructure caused by leaching, thereby enhancing the nanoindentation modulus of the "carbonated + leached zone". Additionally, the presence of cracks is identified adjacent to the "carbonated zone" (Fig. 7C), as an indicator of significant carbonation to some extent.

4.3. Comparison between dry and underwater carbonation

In the case of natural carbonation, Fick's first rule is typically applied to describe the diffusion of CO_2, in which the gradient of CO_2 concentration is the main driving force [58]. However, in addition to the gradient of CO_3^{2-} concentration, Ca^{2+} concentration stands out as another driving force with regard to underwater carbonation. The leaching of Ca^{2+} ions facilitates the carbonation of paste, meanwhile, the carbonation of paste can inversely promote the leaching of Ca^{2+} ions. Despite the synergistic effect of leaching and carbonation, underwater carbonation is milder than natural carbonation, probably because of the slower diffusion of CO_2 under saturated conditions. Nevertheless, it remains essential to pay attention to this issue when the AAS materials are utilized under wet conditions.

5. Conclusions

In this study, the underwater carbonation of AAS pastes subjected to long-term tap water immersion is observed and the underlying mechanisms are revealed. Some conclusions can be summarized as follows.

1. Calcium carbonate is the main CO_2-bearing phase and its content increases with time in AAS pastes subjected to underwater carbonation. Both NH and NS pastes show comparable $CaCO_3$ formation at the same exposure time. Besides, the paste pre-cured for a longer period shows a more severe carbonation, due to a higher reaction degree of slag.
2. The carbonation of hydrotalcite-like phases (Ht-CO_3) is observed in both NH and NS pastes. However, there remains minimal change in the Mg/Al ratio of hydrotalcite upon underwater carbonation, indicating a robust structure of hydrotalcite subjected to water immersion. The gel shows a higher polymerization degree in immersed pastes, due to the gel decalcification induced by both leaching and carbonation. Additionally, the uptake of CO_3^{2-} by gels is also evidenced by TGA-MS results.
3. Due to a coarser microstructure, NH pastes are more vulnerable to underwater carbonation than NS pastes. Long-term tap water immersion results in the leaching of ions, gel decomposition and microstructure deterioration of the paste. However, the leaching of Ca^{2+} ions and the presence of CO_3^{2-} ions in the tap water facilitates the precipitation of calcium carbonate near the exposure front, which can dense the deteriorated microstructure and enhance the indentation modulus of NH pastes.
4. The paste near the exposure front shows a layered distribution. The outmost layer is the carbonated zone, primarily composed of calcium carbonate and formed by the reaction between aqueous CO_3^{2-} ions and Ca^{2+} ions originating from the pastes and tap water. In the intermediate region, there is a transitional zone intermixed by calcium carbonate and leached pastes. The innermost layer near the exposure front is the leached zone, experiencing minimal carbonation but evident leaching. It should be noted that this layer distribution is less evident in NS pastes, as its pore structure is much denser than that of NH pastes.

CRediT authorship contribution statement

Zhenming Li: Writing – review & editing, Supervision. **Guang Ye:** Writing – review & editing, Supervision, Project administration. **Yu Zhang:** Methodology, Investigation. **Minfei Liang:** Methodology, Investigation. **Chen Liu:** Writing – review & editing, Writing – original draft, Methodology, Conceptualization.

Declaration of Competing Interest

The authors declare that they have no known competing financial interests or personal relationships that could have appeared to influence the work reported in this paper.

Data availability

No data was used for the research described in the article.

Acknowledgement

Chen Liu and Minfei Liang would appreciate the funding supported by the China Scholarship Council (CSC) under grants No. 201906950102 and No. 202007000027, respectively. This study is also supported by the Guangdong Provincial Key Laboratory of Intelligent and Resilient Structures for Civil Engineering (2023B1212010004).

Appendix

Fig. A1 shows the morphology of AAS pastes after 90 days of immersion in both deionized and tap water. It can be seen that the sample under deionized water immersion shows a more porous structure near the exposure front compared to the inner part according to the level of the grey scale. However, there is no significant difference observed among samples at different distances from the exposure front in terms of the pore structure.

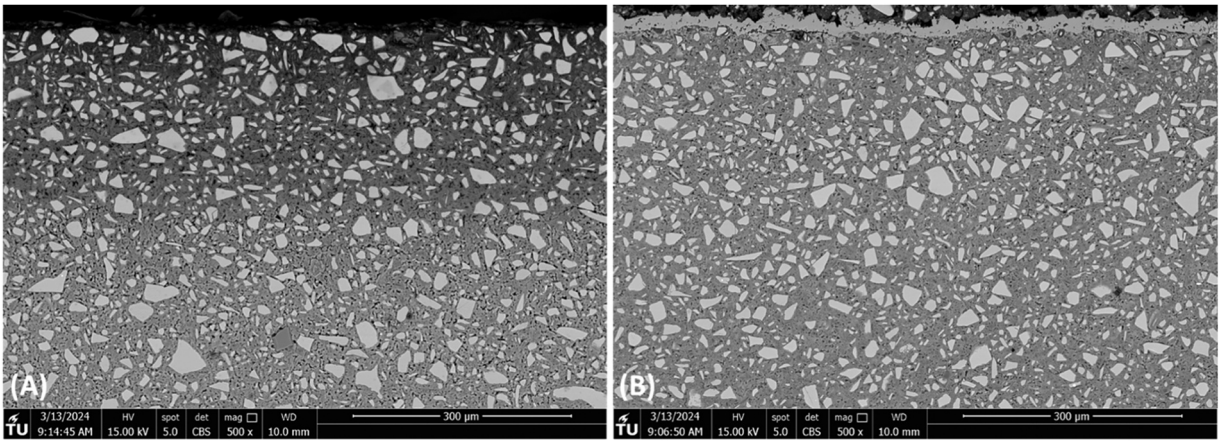

Fig. A1. . SEM images of 28 d AAS pastes subjected to 90 d of immersion in **(A)** deionized water and **(B)** tap water.

References

[1] J.L. Provis, Alkali-activated materials, Cem. Concr. Res. 114 (2018) 40–48, https://doi.org/10.1016/j.cemconres.2017.02.009.

[2] J.L. Provis, A. Palomo, C. Shi, Advances in understanding alkali-activated materials, Cem. Concr. Res. 78 (2015) 110–125, https://doi.org/10.1016/j.cemconres.2015.04.013.

[3] L. Feng, S. Yi, S. Zhao, Q. Zhong, F. Ren, C. Liu, Y. Zhang, W. Wang, N. Xie, Z. Li, N. Cui, Recycling of aluminosilicate-based solid wastes through alkali-activation: preparation, characterization, and challenges, Buildings 14 (2024), https://doi.org/10.3390/buildings14010226.

[4] T. Bakharev, J.G. Sanjayan, Y.B. Cheng, Resistance of alkali-activated slag concrete to carbonation, Cem. Concr. Res. 31 (2001) 1277–1283, https://doi.org/10.1016/S0008-8846(01)00574-9.

[5] N.M. Huang, J.J. Chang, M.T. Liang, Effect of plastering on the carbonation of a 35-year-old reinforced concrete building, Constr. Build. Mater. 29 (2012) 206–214, https://doi.org/10.1016/j.conbuildmat.2011.08.049.

[6] D.M. Kern, The hydration of carbon dioxide, J. Chem. Educ. 37 (1960) 14.

[7] P. Gaikwad, S. Sathe, Effect of fly ash on compressive strength, carbonation and corrosion resistance of reinforced concrete: a systematic review, World J. Eng. (2023), https://doi.org/10.1108/WJE-07-2023-0240.

[8] A. Boucedra, M. Bederina, Effect of plastic aggregates addition on accelerated carbonation of sand concrete, World J. Eng. 20 (2023) 722–731, https://doi.org/10.1108/WJE-10-2021-0606.

[9] S. von Greve-Dierfeld, B. Lothenbach, A. Vollpracht, B. Wu, B. Huet, C. Andrade, C. Medina, C. Thiel, E. Gruyaert, H. Vanoutrive, I.F. Saéz del Bosque, I. Ignjatovic, J. Elsen, J.L. Provis, K. Scrivener, K.C. Thienel, K. Sideris, M. Zajac, N. Alderete, Ö. Cizer, P. Van den Heede, R.D. Hooton, S. Kamali-Bernard, S.A. Bernal, Z. Zhao, Z. Shi, N. De Belie, Understanding the carbonation of concrete with supplementary cementitious materials: a critical review by RILEM TC 281-CCC, 2020. ⟨https://doi.org/10.1617/s11527-020-01558-w⟩.

[10] W. Ashraf, Carbonation of cement-based materials: challenges and opportunities, Constr. Build. Mater. 120 (2016) 558–570, https://doi.org/10.1016/j.conbuildmat.2016.05.080.

[11] C. Liu, X. Liang, Y. Chen, Z. Li, G. Ye, Degradation of alkali-activated slag subject to water immersion, Cem. Concr. Compos. 142 (2022), https://doi.org/10.1016/j.cemconcomp.2023.105157.

[12] N. Li, N. Farzadnia, C. Shi, Microstructural changes in alkali-activated slag mortars induced by accelerated carbonation, Cem. Concr. Res. 100 (2017) 214–226, https://doi.org/10.1016/j.cemconres.2017.07.008.

[13] Z. Shi, B. Lothenbach, M.R. Geiker, J. Kaufmann, A. Leemann, S. Ferreiro, J. Skibsted, Experimental studies and thermodynamic modeling of the carbonation of Portland cement, metakaolin and limestone mortars, Cem. Concr. Res. 88 (2016) 60–72, https://doi.org/10.1016/j.cemconres.2016.06.006.

[14] B. Johannesson, P. Utgenannt, Microstructural changes caused by carbonation of cement mortar, Cem. Concr. Res. 31 (2001) 925–931, https://doi.org/10.1016/S0008-8846(01)00498-7.

[15] J.J. Chen, J.J. Thomas, H.M. Jennings, Decalcification shrinkage of cement paste, Cem. Concr. Res. 36 (2006) 801–809, https://doi.org/10.1016/j.cemconres.2005.11.003.

[16] C. Liu, W. Haoming, L. Zhenming, S. Hu, Y. Guang, Effect of curing condition on mechanical properties and durability of alkali-activated slag mortar, Constr. Build. Mater. 439 (2024) 137376, https://doi.org/10.1016/j.conbuildmat.2024.137376.

[17] S.A. Bernal, R. San Nicolas, R.J. Myers, R. Mejía De Gutiérrez, F. Puertas, J.S.J. Van Deventer, J.L. Provis, MgO content of slag controls phase evolution and structural changes induced by accelerated carbonation in alkali-activated binders, Cem. Concr. Res. 57 (2014) 33–43, https://doi.org/10.1016/j.cemconres.2013.12.003.

[18] G.W. Groves, D.I. Rodway, I.G. Richardson, The carbonation of hardened cement pastes, Adv. Cem. Res. 3 (1990) 117–125.

[19] G. Verbeck, Carbonation of Hydrated Portland Cement, ASTM International West Conshohocken, PA, USA, 1958.

[20] I. Galan, C. Andrade, M. Castellote, Natural and accelerated CO2 binding kinetics in cement paste at different relative humidities, Cem. Concr. Res. 49 (2013) 21–28, https://doi.org/10.1016/j.cemconres.2013.03.009.

[21] M. Fernández Bertos, S.J.R. Simons, C.D. Hills, P.J. Carey, A review of accelerated carbonation technology in the treatment of cement-based materials and sequestration of CO2, J. Hazard. Mater. 112 (2004) 193–205, https://doi.org/10.1016/j.jhazmat.2004.04.019.

[22] Y. Zhang, O. Çopuroğlu, The role of hydrotalcite-like phase and monosulfate in slag cement paste during atmospheric and accelerated carbonation, Cem. Concr. Compos. 132 (2022), https://doi.org/10.1016/j.cemconcomp.2022.104642.

[23] S.A. Bernal, J.L. Provis, D.G. Brice, A. Kilcullen, P. Duxson, J.S.J. Van Deventer, Accelerated carbonation testing of alkali-activated binders significantly underestimates service life: the role of pore solution chemistry, Cem. Concr. Res. 42 (2012) 1317–1326, https://doi.org/10.1016/j.cemconres.2012.07.002.

[24] S.A. Bernal, J.L. Provis, B. Walkley, R. San Nicolas, J.D. Gehman, D.G. Brice, A. R. Kilcullen, P. Duxson, J.S.J. Van Deventer, Gel nanostructure in alkali-activated binders based on slag and fly ash, and effects of accelerated carbonation, Cem. Concr. Res. 53 (2013) 127–144, https://doi.org/10.1016/j.cemconres.2013.06.007.

[25] M. Nedeljković, Y. Zuo, K. Arbi, G. Ye, Carbonation resistance of alkali-activated slag under natural and accelerated conditions, J. Sustain. Metall. 4 (2018) 33–49, https://doi.org/10.1007/s40831-018-0166-4.

[26] S.A. Bernal, J.L. Provis, R. Mejía de Gutiérrez, J.S.J. van Deventer, Accelerated carbonation testing of alkali-activated slag/metakaolin blended concretes: effect of exposure conditions, Mater. Struct. Constr. 48 (2014) 653–669, https://doi.org/10.1617/s11527-014-0289-4.

[27] S.A. Bernal, Effect of the activator dose on the compressive strength and accelerated carbonation resistance of alkali silicate-activated slag/metakaolin blended materials, Constr. Build. Mater. 98 (2015) 217–226, https://doi.org/10.1016/j.conbuildmat.2015.08.013.

[28] E.N. Matteo, B. Huet, C.F. Jové-Colón, G.W. Scherer, Experimental and modelling study of calcium carbonate precipitation and its effects on the degradation of oil well cement during carbonated brine exposure, Cem. Concr. Res. 113 (2018) 1–12, https://doi.org/10.1016/j.cemconres.2018.03.016.

[29] M. Schwotzer, T. Scherer, A. Gerdes, Protective or damage promoting effect of calcium carbonate layers on the surface of cement based materials in aqueous environments, Cem. Concr. Res. 40 (2010) 1410–1418, https://doi.org/10.1016/j.cemconres.2010.05.001.

[30] C. Liu, Z. Li, S. Nie, S. Skibsted, G. Ye, Structural evolution of calcium sodium aluminosilicate hydrate (C-(N-)A-S-H) gels induced by water exposure: the impact of Na leaching, Cem. Concr. Res. 178 (2024), https://doi.org/10.1016/j.cemconres.2024.107432.

[31] O.A. Mohamed, Effects of the curing regime, acid exposure, alkaline activator dosage, and precursor content on the strength development of mortar with alkali-activated slag and fly ash binder: a critical review, Polymers 15 (2023), https://doi.org/10.3390/polym15051248.

[32] R. Snellings, J. Chwast, Ö. Cizer, N. De Belie, Y. Dhandapani, P. Durdzinski, J. Elsen, J. Haufe, D. Hooton, C. Patapy, M. Santhanam, K. Scrivener, D. Snoeck, L. Steger, S. Tongbo, A. Vollpracht, F. Winnefeld, B. Lothenbach, RILEM TC-238 SCM recommendation on hydration stoppage by solvent exchange for the study of hydrate assemblages, Mater. Struct. Constr. 51 (2018), https://doi.org/10.1617/s11527-018-1298-5.

[33] K. Scrivener, R. Snellings, B. Lothenbach, A Pract. Guide Microstruct. Anal. Cem. Mater. (2018), https://doi.org/10.1201/b19074.

[34] M. Liang, Y. Zhang, S. He, Y. Chen, E. Schlangen, B. Šavija, On the chemo-mechanical evolution process of high-volume slag cement paste, Constr. Build. Mater. 400 (2023), https://doi.org/10.1016/j.conbuildmat.2023.132891.
[35] T. Wagner, D.A. Kulik, F.F. Hingerl, S.V. Dmytrieva, GEM-Selektor geochemical modelling package: TSolMod library and data interface for multicomponent phase models, Can. Mineral. 50 (2012) 1173–1195.
[36] D.A. Kulik, T. Wagner, S.V. Dmytrieva, G. Kosakowski, F.F. Hingerl, K. V. Chudnenko, U.R. Berner, GEM-Selektor geochemical modelling package: revised algorithm and GEMS3K numerical kernel for coupled simulation codes, Comput. Geosci. 17 (2013) 1–24, https://doi.org/10.1007/s10596-012-9310-6.
[37] A. Gautschi, J. Becker, D. Traber, W. Leu, Nagra technical report 14-02, geological basics-dossier VII-usage conflicts, Natl. Coop. Dispos. Radioact. Waste (NAGRA) (2014).
[38] W. Hummel, U. Berner, E. Curti, F.J. Pearson, T. Thoenen, Nagra/PSI chemical thermodynamic database 01/01, Radiochim. Acta 90 (2002) 805–813.
[39] B. Lothenbach, D.A. Kulik, T. Matschei, M. Balonis, L. Baquerizo, B. Dilnesa, G. D. Miron, R.J. Myers, Cemdata18: A chemical thermodynamic database for hydrated Portland cements and alkali-activated materials, Cem. Concr. Res. 115 (2019) 472–506, https://doi.org/10.1016/j.cemconres.2018.04.018.
[40] B. Lothenbach, T. Matschei, G. Möschner, F.P. Glasser, Thermodynamic modelling of the effect of temperature on the hydration and porosity of Portland cement, Cem. Concr. Res. 38 (2008) 1–18, https://doi.org/10.1016/j.cemconres.2007.08.017.
[41] T. Matschei, B. Lothenbach, F.P. Glasser, Thermodynamic properties of Portland cement hydrates in the system CaO-Al2O3-SiO2-CaSO4-CaCO3-H2O, Cem. Concr. Res. 37 (2007) 1379–1410, https://doi.org/10.1016/j.cemconres.2007.06.002.
[42] R.J. Myers, S.A. Bernal, J.L. Provis, A thermodynamic model for C-(N-)A-S-H gel: CNASH-ss. Derivation and validation, Cem. Concr. Res. 66 (2014) 27–47, https://doi.org/10.1016/j.cemconres.2014.07.005.
[43] R.J. Myers, B. Lothenbach, S.A. Bernal, J.L. Provis, Thermodynamic modelling of alkali-activated slag cements, Appl. Geochem. 61 (2015) 233–247, https://doi.org/10.1016/j.apgeochem.2015.06.006.
[44] A. Fernández-Jiménez, F. Puertas, I. Sobrados, J. Sanz, Structure of calcium silicate hydrates formed in alkaline-activated slag: Influence of the type of alkaline activator, J. Am. Ceram. Soc. 86 (2003) 1389–1394, https://doi.org/10.1111/j.1151-2916.2003.tb03481.x.
[45] M. Ben Haha, G. Le Saout, F. Winnefeld, B. Lothenbach, Influence of activator type on hydration kinetics, hydrate assemblage and microstructural development of alkali activated blast-furnace slags, Cem. Concr. Res. 41 (2011) 301–310, https://doi.org/10.1016/j.cemconres.2010.11.016.
[46] G. Villain, M. Thiery, G. Platret, Measurement methods of carbonation profiles in concrete: thermogravimetry, chemical analysis and gammadensimetry, Cem. Concr. Res. 37 (2007) 1182–1192, https://doi.org/10.1016/j.cemconres.2007.04.015.
[47] Z. Shi, C. Shi, S. Wan, N. Li, Z. Zhang, Effect of alkali dosage and silicate modulus on carbonation of alkali-activated slag mortars, Cem. Concr. Res. 113 (2018) 55–64, https://doi.org/10.1016/j.cemconres.2018.07.005.
[48] E. Bernard, W.J. Zucha, B. Lothenbach, U. Mäder, Stability of hydrotalcite (Mg-Al layered double hydroxide) in presence of different anions, Cem. Concr. Res. 152 (2022), https://doi.org/10.1016/j.cemconres.2021.106674.
[49] A. Morandeau, M. Thiéry, P. Dangla, Investigation of the carbonation mechanism of CH and C-S-H in terms of kinetics, microstructure changes and moisture properties, Cem. Concr. Res. 56 (2014) 153–170, https://doi.org/10.1016/j.cemconres.2013.11.015.
[50] M. Palacios, F. Puertas, Effect of carbonation on alkali-activated slag paste, J. Am. Ceram. Soc. 89 (2006) 3211–3221.
[51] F. Spectroscopy, Struct. Calcium Silic. Hydrate (C. -S-H.): -, -, Far-Infrared Spectrosc. 48 (1999) 742–748.
[52] J.J. Chen, J.J. Thomas, H.F.W. Taylor, H.M. Jennings, Solubility and structure of calcium silicate hydrate, Cem. Concr. Res. 34 (2004) 1499–1519, https://doi.org/10.1016/j.cemconres.2004.04.034.
[53] A. Vidmer, G. Sclauzero, A. Pasquarello, Infrared spectra of jennite and tobermorite from first-principles, Cem. Concr. Res. 60 (2014) 11–23, https://doi.org/10.1016/j.cemconres.2014.03.004.
[54] Y. Zhang, M. Liang, Y. Gan, O. Çopuroğlu, Effect of MgO content on the quantitative role of hydrotalcite-like phase in a cement-slag system during carbonation, Cem. Concr. Compos. 134 (2022), https://doi.org/10.1016/j.cemconcomp.2022.104765.
[55] F. Cihangir, B. Ercikdi, A. Kesimal, S. Ocak, Y. Akyol, Effect of sodium-silicate activated slag at different silicate modulus on the strength and microstructural properties of full and coarse sulphidic tailings paste backfill, Constr. Build. Mater. 185 (2018) 555–566, https://doi.org/10.1016/j.conbuildmat.2018.07.105.
[56] Y. Zhang, S. Zhang, C. Liu, O. Çopuroğlu, Characterizing two types of zonation within slag rims of aged alkali-activated slag pastes through SEM and TEM, Cem. Concr. Res. 176 (2024) 107409, https://doi.org/10.1016/j.cemconres.2023.107409.
[57] A. Machner, M. Zajac, M. Ben Haha, K.O. Kjellsen, M.R. Geiker, K. De Weerdt, Stability of the hydrate phase assemblage in Portland composite cements containing dolomite and metakaolin after leaching, carbonation, and chloride exposure, Cem. Concr. Compos. 89 (2018) 89–106, https://doi.org/10.1016/j.cemconcomp.2018.02.013.
[58] X. Zha, M. Yu, J. Ye, G. Feng, Numerical modelling of supercritical carbonation process in cement-based materials, Cem. Concr. Res. 72 (2015) 10–20, https://doi.org/10.1016/j.cemconres.2015.02.017.